Measurement of Cavitation in a Sliding Bearing using Digital Holography

Tian TANG [1,*], Laura AREVALO [2], Jeremy M COUPLAND [1]

* Corresponding author: Tel.: ++44 (0)1509 227519; Email: T.tang2@lboro.ac.uk
1 Department of Mechanical and Manufacturing Engineering, Loughborough University. UK
2 Aragón Institute of Engineering Research, University of Zaragoza, Spain

Abstract Although most of the mathematical models for cavitation in bearings provide reasonable estimates of engineering parameters such as load capacity and friction, they are based on substantially different assumptions and further work is required to understand the fundamental operation of bearings. In this study digital holography was used to examine bubble formation within a glass sliding bearing. Digital holography collects the both the phase and amplitude of the transmitted wavefront and therefore contains quantitative information concerning the thickness of the cavitation bubbles. This paper introduces the experimental configuration and the digital holography system used to study cavitation. It also discusses the demodulation process and how the information can be used to find other interesting parameters such as bubble position and shape.

Keywords: Digital holography, Cavitation, Sliding bearing, Piston ring, Bubble

1. Introduction

It is well known that cavitation bubbles are observed in fluid flow when the local pressure falls below the vapor pressure or saturation pressure of a liquid and are most frequently associated with the erosion of the marine propellers and pump impellers. In 1886, however, Osborne Reynolds suggested that cavitation is also possible in the shear-driven lubricating flow between bearing surfaces [1] and since then considerable effort has been applied to the understanding and modeling of sliding or rolling contact bearings. For the case of a convergent/divergent sliding bearing, the pressure distribution, *p(x)*, is typically related to height profile, *h(x)*, and the velocity of the bearing surfaces, u_1 and u_2 by the one-dimensional Reynolds equation,

$$\frac{d}{dx}\left(\frac{h^3}{\eta}\frac{dp}{dx}\right)=6(u_1+u_2)\frac{dh}{dx} \qquad (1)$$

where η is the viscosity [1]. The Reynolds equation is then solved, assuming various boundary conditions and this is the basis of many bearing load models. The simplest of these models ignore mass flow continuity and either assume that film rupture (cavitation) occurs at the beginining of the divergent zone, as in the Gumbel model [2], or where the pressure gradient equal to zero as in the Swift and Stieber model [3,4]. In order to account for mass flow continuity two-dimensional aspects of the flow must be considered. In line with experimental observation, the JFO (Jakobson, Floberg and Olsson) model [5] assumes that film rupture occurs in separate cavities (cavitation bubbles) that occupy the whole space between the bearing surfaces and the lubricant flows in the region between the bubbles. In Coyne and Elrod's model [6], however, mass flow continuity is satisfied by flow over the cavity such that the lubricating film is never completely ruptured.

Although the pressure distributions predicted by the various models differ slightly they all provide reasonable estimates of steady state engineering parameters such as load capacity and friction. Significant differences are apparent in transient events, however, (e.g.

piston ring reversal) and for this reason further work is required to understand the fundamental cavitation process.

In this paper we consider preliminary use of digital holographic microscopy to measure the size and position of cavitation bubbles in sliding bearings. Digital holographic microscopy is a powerful method that has been used measure flow in microfluidic devices [7] . The technique essentially measures both the phase and amplitude of the scattered wavefront and in this case, it is this that carries the information concerning the position and thickness of the cavitation. Furthermore, in certain circumstances digital microscopy has the ability to correct for optical aberrations introduced during the imaging process and in this in this study, the spherical aberration that is introduced by the comparatively thick glass used in the optical setup.

Section 2 of this paper introduces the experimental configuration. The digital holographic microscope and the reconstruction process are outlined in section 3 and measurement of the thickness and position of cavitation bubbles in section 4. Section 5 discusses the results with reference to the one-dimensional bearing load models and the future extension of this work to include direct measurement of the lubricating flow is outlined in section 6.

2. Experimental configuration

Figure 1 shows the glass sliding bearing that generates a lubricating flow which is functionally similar to that between a lubricated piston ring and the cylinder liner in a reciprocating IC engine. In this case the sliding contact is between a cylindrical lens and a plane glass surface. The lubricating oil is additive-free, high viscosity green gear oil (SAE 140). The plane glass is driven by a motorized translation stage capable of bi-directional motion with controlled speed (0 mm/s - 2.3 mm/s) and acceleration (up to 1.50 mm/s^2). Under these conditions the thickness of the lubricating film is between 0.3 μm and 10 μm and the cavitation bubbles are typically up to 500 μm in length.

Figure 2 shows the experimental configuration and the light transmission path. A rectangular aperture (20 mm $\times 5$ mm) on the motorized translation stage allows the laser illumination to pass and provides sufficient

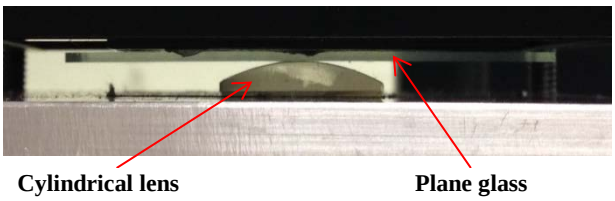

Figure 1 Experimental configuration.

support to the plane surface. A second 10 mm diameter circular aperture below the stationary cylindrical part allows the scattered light to be collected over a large numerical aperture (NA).

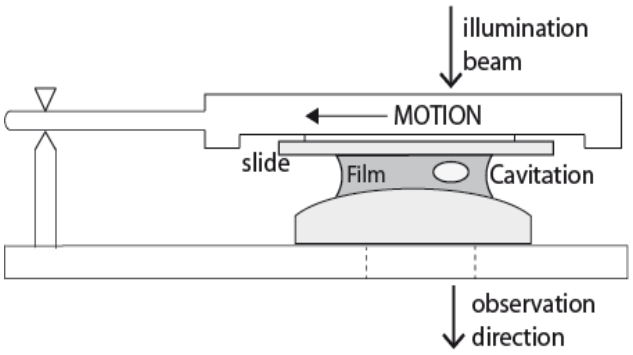

Figure 2 Optical path through the experimental configuration.

3. Digital holographic microscopy

The digital holographic microscope that was used for this study is shown in figure 3. The plane wave from a diode pumped, frequency doubled Nd:YLF laser of wavelength λ =523 nm is divided into reference and object beams using a 50:50 beam splitter. The bearing is illuminated by the plane wave that constitutes the object beam and its image magnified by 80$\times$ using a microscope objective with NA=0.55. The image is mixed with a diverging reference wave from the same source such that a near image-plane hologram is recorded on a CCD

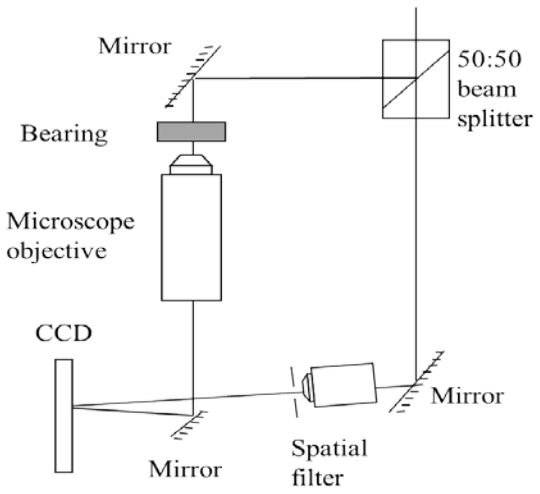

Figure 3 Digital holography system.

sensor with 4008×2672, $9.0\ \mu m$ square pixels. Details of this microscope and the reconstruction process can be found elsewhere [8, 9], however, it is worth considering some of the fundamental attributes of a coherent imaging system such as this.

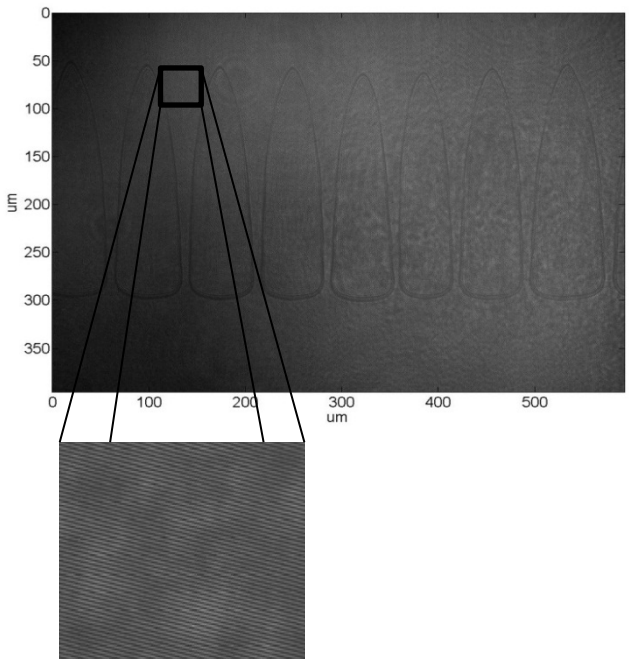

Figure 4 Holographic recording of cavitation.

The fundamental difference between incoherent and coherent imaging is illustrated by figure 4 which shows the intensity pattern recorded by the CCD. An enlargement of the black square reveals the fringes caused by the interference of the object beam and the reference beam. It is the position and strength of these fringes that contain the information that is related to the amplitude and the phase of the recorded wavefront. In order to reconstruct the hologram the following demodulation process is used.

If the complex field due to the illuminating passing through the glass bearing is $\mathbf{o}(x, y)$ and the complex reference field is $\mathbf{r}(x, y)$, then the intensity of figure 4, $I(x, y)$, can be written as

$$I(x, y) = \left|\mathbf{r}(x, y) + \mathbf{o}(x, y)\right|^2 = \left|\mathbf{r}(x, y)\right|^2 + \left|\mathbf{o}(x, y)\right|^2 + \mathbf{o}(x, y)^* \mathbf{r}(x, y) + \mathbf{o}(x, y)\mathbf{r}(x, y)^* \quad (2)$$

In off-axis holography, each of the terms has different spatial bandwidth which means in equation (2) each terms can be separated in the frequency domain. Figure 5 is the absolute value of the Fourier transform of figure 4 which illustrates the frequency bands corresponding to the different terms in equation (2). The center circle represents the band of first two terms in equation (2) while the two bright regions in the corners of the spectrum represent the holographic image of the third and fourth terms respectively.

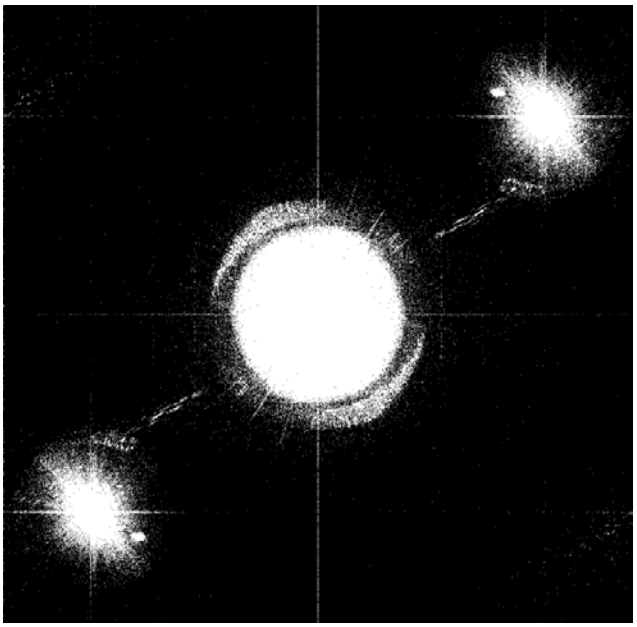

Figure 5 Fourier spectrum of the hologram.

Holographic reconstruction can be achieved using the Fourier transform of either the third or fourth term. Since the reference field is known the phase and amplitude of object field can be calculated. Hence, the reconstruction is simply a filtered version of the recorded intensity pattern.

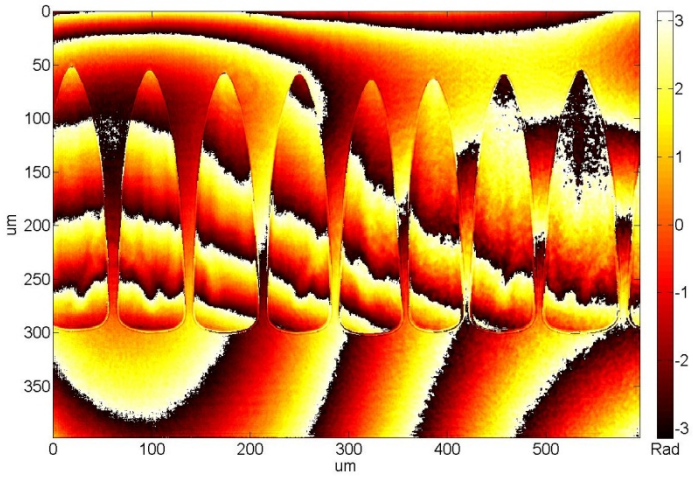

Figure 6 Demodulate phase map.

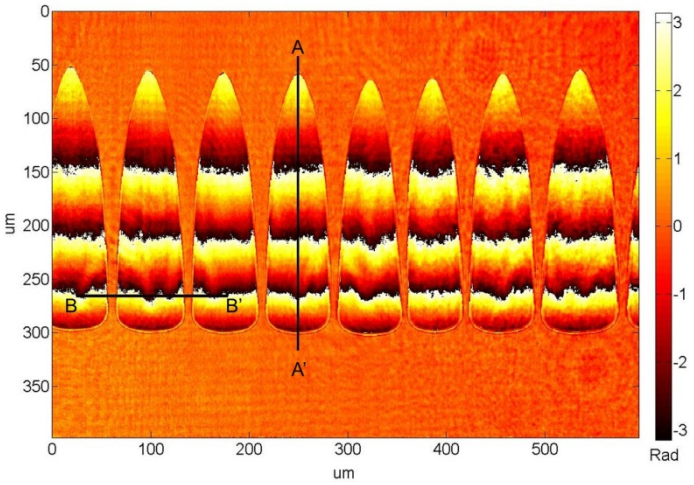

Figure 7 Subtracted phase map.

A major advantage of coherent imaging using digital holographic microscopy rather than its incoherent counterpart is that both the recorded fields are available for further analysis. That is the recovered object field, $\mathbf{o}(x, y)$ can be written,

$$\mathbf{o}(x, y) = a(x, y)\exp(\mathbf{j}\phi(x, y)) \qquad (3)$$

where $\phi(x, y)$ is the phase and $a(x, y)$ the amplitude distribution. In this study the phase is the most important parameter as illustrated in figure 6 which shows the phase of the demodulated hologram shown in figure 4. It can be seen that the cavitation bubbles are revealed but there are underlying fringes that are principally due to wavefront aberration in the illuminating beam. In order to remove this contribution it is useful to subtract the phase distribution recovered from a holographic recording of the apparatus when there is no cavitation (i.e. when the slide is stationary).

An example of the subtracted phase is shown in figure 7. The figure will be discussed further in section 4 but it is noted here that the cavitation bubbles are generated by the motorized translation stage moving from top to bottom.

In this case, the direction of the oil flow is also from top to bottom. Hence, figure 7 shows that the gap between the bubbles is greater upstream and narrows downstream as the clearance between the bearing surfaces increases. This appears to be in accordance with continuity of mass flow around the cavitation bubbles. In the following section we consider quantitative measurement of the thickness and position of the cavitation bubbles

4. Bubble thickness and position

A quantitative measurement of bubble thickness can be made from the fringes within the subtracted phase shown in figure 7. An elementary analysis shows that the change in phase, $\Delta\varphi$ due to propagation of the illuminating wave through a distance $T(x, y)$ in the cavitation bubble is given by

$$\Delta\varphi(x, y) = \frac{2\pi}{\lambda}(n_0 - 1)T(x, y) \qquad (4)$$

Using the published refractive index of the classic green gear oil (1.499) the thickness profile of the cavitation bubble along the line A-A' shown in figure 7 is illustrated in figure 8.

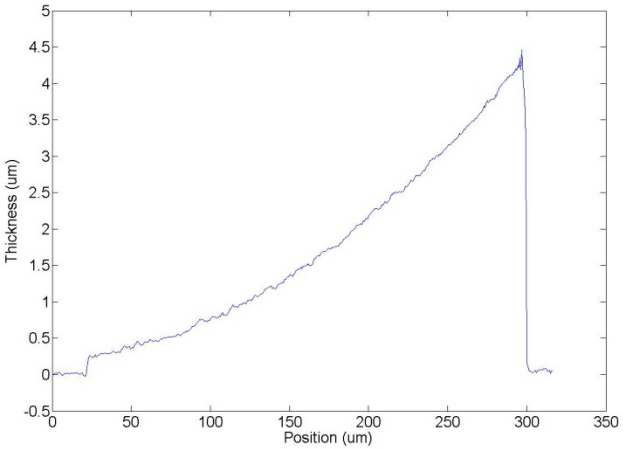

Figure 8 Bubble thickness along the line A-A' in figure 7.

It is interesting to note that at the upstream end of the bubble the profile jumps to a thickness of about 300 nm within the system resolution. The bubble thickness increases in this case to around 4.5 μm where once again there is a step change in thickness that is not resolved by the system. This implies that the radius of curvature is smaller than the resolution at this point (approximately 2 pixels == 1 μm).

We will return to these findings and their consequences later, however, for the moment let us consider the bubble position further. As mentioned in section 2, the experimental setup allows has the capability to reverse the direction of the movement and this allows the position of the bubbles relative to the line of minimum clearance to be found. Figures 9 (a) – (d) show the addition the phase distributions for forward and reverse motion at different velocities. It is noted that at higher shear velocity the bubbles form a stable regular pattern whereas at lower velocity the number of bubbles increases and they have an irregular "fir tree" like appearance. By their nature, the one-dimensional models discussed previously do not account for the bubble shape and contain no information regarding the apparent complexity of bubble generation.

The line of symmetry, however, allows the line of minimum clearance to be found and is marked by dots in the figure 9 (a). It is noted

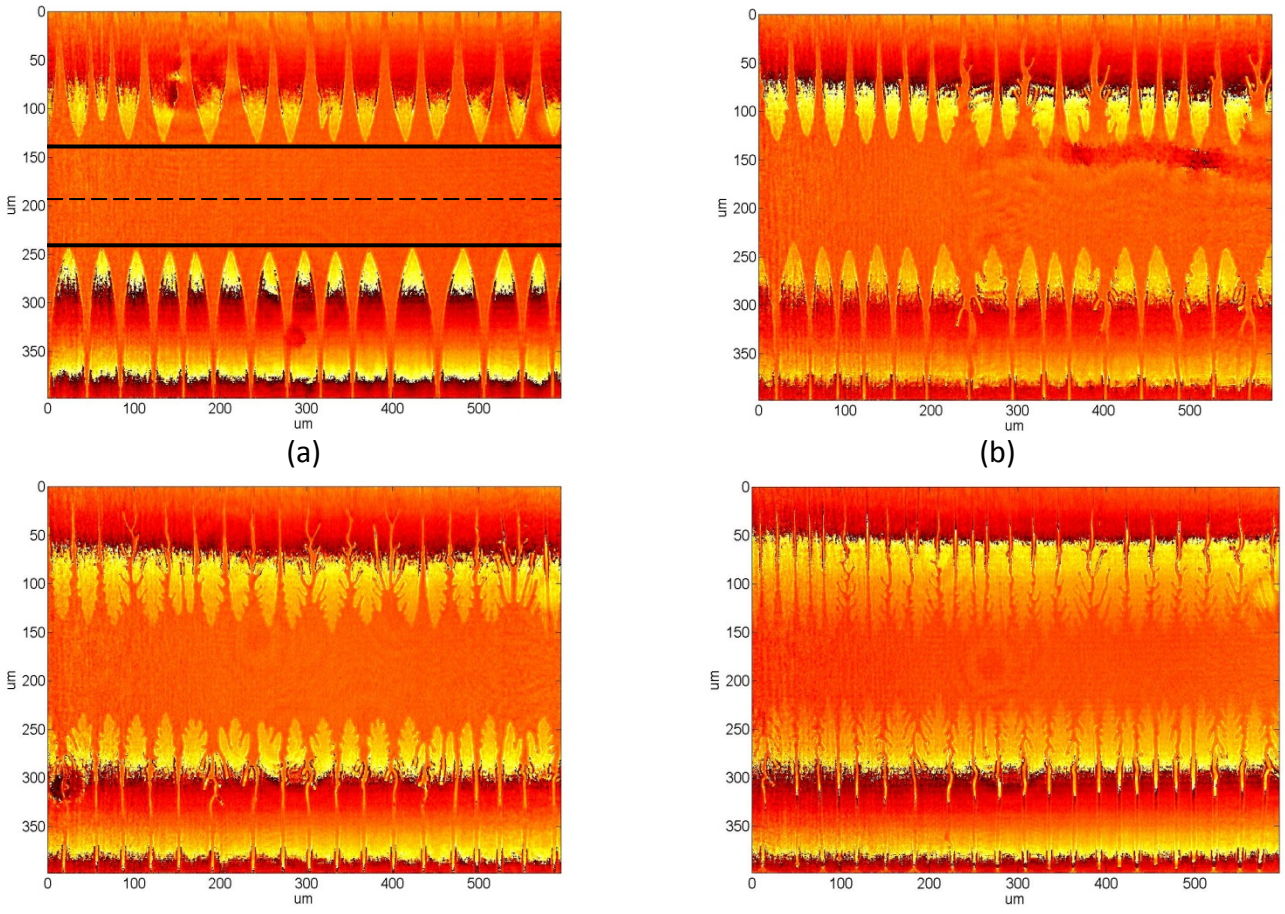

Figure 9 Addition of forward and reverse phase maps at: (a) 2.0 mm/s; (b)1.5 mm/s; (c) 1.0mm/s; (d) 0.5 mm/s.

that as the speed increases the cavitation moves toward the line of minimum clearance. This finding shows that the fundamental assumption of Gumbel's model is inaccurate. The distance from the onset of cavitation has been compared with that calculated using the more comprehensive JFO model and is shown in figure 10. It can be seen that although the theoretical trend is followed the bubble formation occurs at a point 30-40% greater than that predicted by the JFO model.

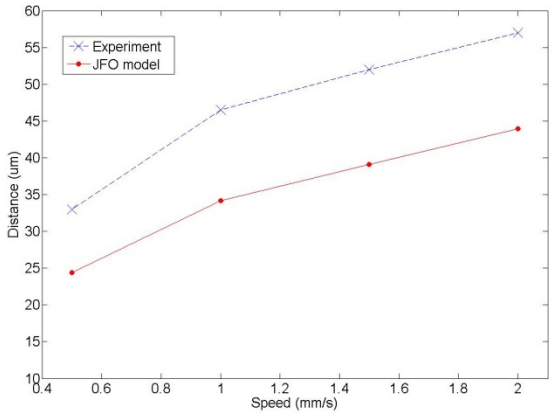

Figure 10 Distance from minimum clearance to bubble formation versus speed.

It is clear that the phase distributions calculated from the digital holograms provide valuable information concerning the thickness and lateral position of the bubble, however, it is also possible to deduce something about the axial position of the bubbles from this data.

First, it is noted that stable bubbles must be in contact with at least one of the bearing surfaces. This follows from the Laplace-Young equation that states that the pressure within a bubble, Δp, such that,

$$\Delta p = \gamma \left(\frac{1}{R_1} + \frac{1}{R_2} \right) \qquad (5)$$

where γ is the surface tension and $R_1$and R_2 are the principal radii of curvature [10,11]. The surface tension of the gear oil is presently unknown but using a typical value for this type of mineral oil γ = 32.5 mN/m it is found that for the bubble pressure to exceed atmospheric pressure either of the principal radii must exceed 325 nm . Since the minimum thickness of the bubble (figure 8) is of a similar order it follows that the bubbles must be in contact with at least one of the bearing surfaces and there cannot be free bubbles in the lubricant if the process is in dynamic equilibrium.

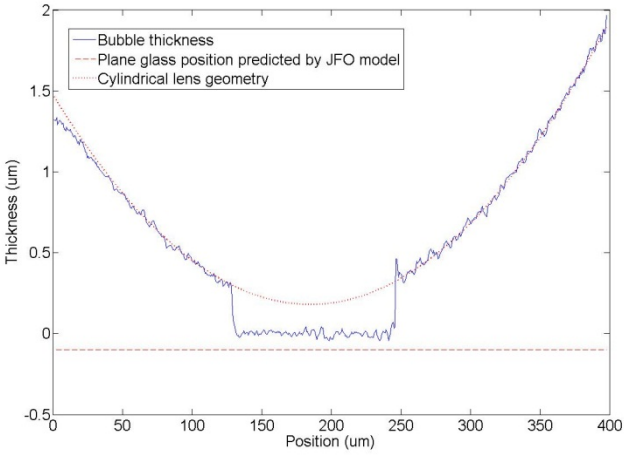

Figure 11 Bubble thickness measurement with reference to the cylindrical sand plane surfaces.

There is evidence however, that supports the hypothesis that the bubble does not span the whole distance between the bearing surfaces. Further inspection of the phase distribution illustrated in figure 7 shows that there is a wave like change in bubble thickness along the line B-B'. This implies that there is fluid on one side of the bubble as assumed in Coyne and Elrod's model [6]. It is interesting to combine this information with our knowledge of the form of the cylindrical surface (radius = 13.25 mm). Figure 11 shows the position of cavitation bubbles for both forward and reverse velocity of 2 mm/s under the assumption that they are in contact with the cylindrical profile. It is interesting to note that the bubble thickness is such that the lower surface of the bubble is almost flat (but it is not in contact with the plane glass for the reasons mentioned previously). Although, at present we cannot reliably measure the distance between the bearing surfaces, we can calculate this distance using for example the JFO model. In figure 11 the position of the plane surface is marked accordingly. It can be seen that the position is consistent with the hypothesis that there is a continuous

lubricating film between the bearing surface (i.e. the film is not fully ruptured).

5. Conclusions

This paper has discussed the measurement of cavitation bubbles in sliding bearings using digital holography. In contrast with incoherent imaging methods digital holography records the phase and amplitude of the transmitted wavefront. Using this information it is possible to compensate for aberrations in the system (in this case severe spherical aberration), providing high resolution phase images and measurements of bubble thickness. The preliminary findings have been compared with the various theoretical models based on the 1D Reynolds equation.

The apparatus used for this work allowed careful control of the speed and direction of a cylindrical sliding bearing lubricated by high viscosity gear oil. Using an argument based on symmetry it was possible to establish the position of the cavitation bubbles with respect to the line of minimum clearance. Although this measurement followed the same trend the position was 30-40% greater than that predicted by the JFO model.

The bubble thickness measurements can also be used to deduce the axial position of the bubbles and establish whether the cavities extend between the bearing surfaces (as assumed in the JFO model) or contact a single surface (as assumed by Coyne and Elrod's model). The thickness results show that the thickness profile closely follows that of the cylindrical bearing surface and consideration of the bubble pressure (as predicted by the Laplace-Young equation) suggests that the cavitation must contact at least one of the bearing surfaces. Close examination of the thickness variation shows that there is indeed a "wavy" lubrication film that by inference can be assumed to be in contact with the plane surface.

From the evidence collected in this study it appears that the assumptions of Coyne and Elrod's model most closely match fundamental processes that define lubricating flow. It is noted however, that the model is a 1D representation of the flow. The experimental data clearly shows the 2D (and possibly 3D) nature of the cavitation process in lubricating flow. In particular, figure 9 shows the beautiful "fir tree" like structures that are observed at low speeds and at the onset of the cavitation process. These structures are dynamic and often show a high degree of symmetry.

In order to understand the cavitation process further work is planned to measure the flow velocity within the lubricating fluid (using stabilized nano-particles) and to establish the position of the bearing surfaces more accurately using interferometry.

References

1. REYNOLDS, O. 1886. On the theory of lubrication and its application to Beauchamp Tower's experiments, Including an experimental determination of the viscosity of olive oil. *Philos. Trans. R. Soc. London Ser. A 177:157-233.*
2. GÜMBEL, L. K. R. 1921. Vergleich der Ergebrusse der rectinerischen Behandling des Lagerschmierangsproblem mitneueren Versuchsergebrussen. *Monatsbl. Berliner Bez. Ver. Dtsch. Ing., 125-128.*
3. SWIFT, W. 1933. The stability of lubricating film in journal bearing. *J. Inst. Civ. Eng. 233 (Pt. 1): 267-88.*
4. STIEBER, W. 1933. *Das Schwimmlager. Berlin: Ver. Dtsch. Ing.*
5. FLOBERG, L. 1974. Cavitation Boundary Condition with Regard to the Number of Streamers and Tensile Strength of the Liquid. *Cavitation and Related Phenomena in Lubrication, ImechE, England, pp. 31-36.*
6. COYNE, J. and ELROD JR, H. 1971. Condition for the Rupture of a Lubricating Film-Part II: New Boundary Condition for Reynolds Equation. *Journal of Lubrication Technology, vol. 93, pp. 156.*
7. SCHNARS, U., and JUPTNER, W. P. 2002. Digital recording and numerical reconstruction of holograms. *Measurement science and technology, 13(9), R85.*
8. WORMALD, S. A., and COUPLAND, J. M. 2009. Particle image identification and

correlation analysis in microscopic holographic particle image velocimetry. *Applied optics 48.33: 6400-6407.*

9. LOBERA, J., and COUPLAND, J. M. 2008. Contrast enhancing techniques in digital holographic microscopy. *Measurement Science and Technology, 19(2), 025501*.
10. LAPLACE, P.S., 1806 *Méchanique céleste*, suppl. 10th vol.
11. YOUNG, T. 1805. Philos. Trans. R. Soc. London 95, 65.